



HAL
open science

Mantle oxidation by sulfur drives the formation of giant gold deposits in subduction zones

Deng-Yang He, Kun-Feng Qiu, Adam Simon, Gleb S. Pokrovski, Hao-Cheng Yu, James Connolly, Shan-Shan Li, Simon Turner, Qing-Fei Wang, Meng-Fan Yang, et al.

► **To cite this version:**

Deng-Yang He, Kun-Feng Qiu, Adam Simon, Gleb S. Pokrovski, Hao-Cheng Yu, et al.. Mantle oxidation by sulfur drives the formation of giant gold deposits in subduction zones. Proceedings of the National Academy of Sciences of the United States of America, 2024, 121 (52), pp.e2404731121. 10.1073/pnas.2404731121 . hal-04911444

HAL Id: hal-04911444

<https://hal.science/hal-04911444v1>

Submitted on 24 Jan 2025

HAL is a multi-disciplinary open access archive for the deposit and dissemination of scientific research documents, whether they are published or not. The documents may come from teaching and research institutions in France or abroad, or from public or private research centers.

L'archive ouverte pluridisciplinaire **HAL**, est destinée au dépôt et à la diffusion de documents scientifiques de niveau recherche, publiés ou non, émanant des établissements d'enseignement et de recherche français ou étrangers, des laboratoires publics ou privés.



Distributed under a Creative Commons Attribution 4.0 International License

1

2

3 Main Manuscript for

4 Mantle oxidation by sulfur drives the formation of giant gold deposits in 5 subduction zones

6

7 Deng-Yang He¹, Kun-Feng Qiu^{1,2*}, Adam C. Simon³, Gleb S. Pokrovski², Hao-Cheng Yu¹, James A.
8 D. Connolly⁴, Shan-Shan Li⁵, Simon Turner⁶, Qing-Fei Wang¹, Meng-Fan Yang¹, Jun Deng^{1,7*}

9 ¹ Frontiers Science Center for Deep-time Digital Earth, State Key Laboratory of Geological
10 Processes and Mineral Resources, School of Earth Sciences and Resources, China University of
11 Geosciences, Beijing, 100083, China

12 ² Experimental Geosciences Team, Géosciences Environnement Toulouse (GET), Observatoire
13 Midi-Pyrénées, Université de Toulouse III Paul Sabatier, Centre National de la Recherche
14 Scientifique (CNRS), Institut de Recherche pour le Développement (IRD), 14, avenue Edouard
15 Belin, F-31400 Toulouse, France

16 ³ Department of Earth and Environmental Sciences, University of Michigan, Ann Arbor, MI, USA

17 ⁴ Department of Earth Sciences, ETH Zurich, Zürich, Switzerland

18 ⁵ School of Science, China University of Geosciences, Beijing 100083, China

19 ⁶ Department of Earth and Environmental Sciences, Macquarie University, Sydney 2109, Australia

20 ⁷ Geological Research Institute of Shandong Gold Group Co., Ltd., Jinan 250013, China

21 * Kun-Feng Qiu, Jun Deng

22 **Email:** kunfengqiu@qq.com, djun@cugb.edu.cn

23 **Author Contributions:** K.F.Q and D.Y.H conceived the project and processed the modeling
24 results. J.A.D.C developed the Perple_X software for the slab devolatilization and mantle infiltration
25 calculations. D.Y.H and G.S.P performed the geochemical modeling of Au solubility. M.F.Y, H.C.Y
26 and D.Y.H performed the data collection and drafted the figures. J.D, K.F.Q, A.C.S and G.S.P
27 acquired funding and contributed to the conceptualization. D.Y.H and K.F.Q wrote the original
28 manuscript with contributions from A.C.S, G.S.P, J.A.D.C, S.S.L, S.T and Q.F.W. All authors
29 analyzed and discussed the data, and revised the manuscript.

30 **Competing Interest Statement:** The authors declare that they have no known competing financial
31 interests or personal relationships that could have appeared to influence the work reported in this
32 paper.

33 **Classification:** Physical Sciences/ Earth, Atmospheric, and Planetary Sciences

34 **Keywords:** sulfur redox, oxygen fugacity, mantle wedge, gold deposits, subduction zone

35

36 **This PDF file includes:**

37 Main Text

38 Figures 1 to 5

39

40 **Abstract**

41 Oxidation of the sub-arc mantle driven by slab-derived fluids has been hypothesized to
42 contribute to the formation of gold deposits in magmatic arc environments that host the majority of
43 metal resources on Earth. However, the mechanism by which the infiltration of slab-derived fluids
44 into the mantle wedge changes its oxidation state and affects Au enrichment remain poorly
45 understood. Here we present the results of a numerical model that demonstrates that slab-derived
46 fluids introduce large amounts of sulfate (S^{6+}) into the overlying mantle wedge that increase its
47 oxygen fugacity by up to 3 to 4 log units relative to the pristine mantle. Our model predicts that as
48 much as 1 wt.% of the total dissolved sulfur in slab-derived fluids reacting with mantle rocks is
49 present as the trisulfur radical ion, S_3^- . This sulfur ligand stabilizes the aqueous $Au(HS)S_3^-$ complex,
50 which can transport Au concentrations of several grams per cubic meter of fluid. Such
51 concentrations are more than three orders of magnitude higher than the average abundance of Au
52 in the mantle. Our data thus demonstrate that an aqueous fluid phase can extract 10–100 times
53 more Au than in a fluid-absent rock-melt system during mantle partial melting at redox conditions
54 close to the sulfide-sulfate boundary. We conclude that oxidation by slab-derived fluids is the
55 primary cause of Au mobility and enrichment in the mantle wedge and that aqueous fluid-assisted
56 mantle melting is a prerequisite for formation of Au-rich magmatic-hydrothermal and orogenic gold
57 systems in subduction zone settings.

58 **Significance Statement**

59 Upon subduction, the oceanic crust releases aqueous fluids that infiltrate the overlying mantle.
60 Compared to primitive mantle, this metasomatized mantle is enriched in gold and other economic
61 metals to provide a source for mineral deposits. However, the fundamental causes of metal
62 enrichment remain enigmatic. We demonstrate that sulfur is the key agent causing Au enrichment in
63 the fluid upon its reaction with the mantle, by forming the soluble $Au(HS)S_3^-$ complex. This species
64 concentrates in fluid up to 1000 times more Au than its average mantle abundance. This gold
65 enrichment in fluid is a key condition for forming Au-rich melts by fluid-present mantle melting. Our
66 work provides the first quantitative assessment of the behaviors of sulfur and gold during
67 subduction-related processes.

68 **Main Text**

69 **Introduction**

70 Subduction zones are the main regions of mass exchange between the mantle and crust on
71 Earth. In particular, metals, water and other volatiles are transferred from the subducting slab to
72 overlying mantle wedge by fluids (1-3) and melts (4, 5). These fluids and melts are considered to be
73 oxidized relative to those from the pristine mantle beneath the mid-ocean ridges (6). Different arc
74 magma geochemical signatures, such as elevated total boron concentrations and $\delta^{11}B$ values (7)
75 along with enrichment in large-ion lithophile elements (8) mirror those of the subducted oceanic
76 slab, suggesting a connection between mantle wedge oxidation and the input of slab-related
77 components (6). Thus, metasomatized peridotite xenoliths from the sub-arc mantle record oxygen
78 fugacity values up to 2 log units higher than those of the conventional fayalite-magnetite-quartz
79 buffer ($\log(fO_2)$ from $\Delta FMQ-1$ to $\Delta FMQ+2$) (9-11). Such redox conditions support the hypothesis
80 that slab-derived fluids oxidize the mantle wedge.

81 Because oxidized sulfur (S^{4+} and S^{6+}), present as sulfate and sulfite species (HSO_4^- , SO_4^{2-} ,

82 HSO₃⁻, SO₂) and their ion pairs with major cations (Na, K, Ca, Mg), is believed to be soluble in high-
83 pressure aqueous fluids, infiltration of such fluids may explain why the sub-arc mantle wedge would
84 be oxidized relative to depleted mantle (12-15). The input of sulfate-bearing slab-derived fluids is
85 also supported by elevated δ³⁴S values in arc lavas (16, 17). Oxidizing agents such as sulfate and
86 ferric iron are thought to be required for resorption of Au-bearing sulfides during partial melting of
87 the mantle wedge (11, 18, 19), making such oxidation phenomena essential for the formation of
88 porphyry and orogenic gold deposits. However, compared to more reduced sulfur species such as
89 HS⁻, H₂S, and S₃⁻, which are major sulfur ligands for transporting Au in aqueous fluids (20, 21),
90 sulfate has little capacity to form Au complexes. Because of a lack of quantitative assessment of the
91 impact of such sulfur-mediated redox reactions both on the oxidation state of the mantle wedge and
92 gold solubility in aqueous fluids and silicate melts originating from the metasomatized mantle, it is
93 unclear how these opposing factors can be reconciled to explain gold transport within the mantle
94 wedge.

95 Here we report the results of thermodynamic simulations that quantitatively predict the
96 chemistry of fluids generated by prograde devolatilization of subducted oceanic crust. We show that
97 the resulting sulfate-bearing fluids oxidize ferrous iron in the silicate minerals within the mantle
98 wedge. As a consequence of this oxidation, the fluid becomes reduced and enriched in trisulfur
99 radical ion, S₃⁻, which forms soluble complexes such as Au(HS)S₃⁻ with Au. We propose that this
100 sulfur-driven redox phenomenon is the fundamental mechanism of Au enrichment in magmatic arcs
101 that host a major proportion of global economic resources of gold. These findings highlight that
102 mantle oxidation improves the recycling efficiency of volatiles and metals in subduction zones.

103 **Results**

104 ***Devolatilization of altered oceanic crust and sulfur mobility***

105 Results from the devolatilization models (see Materials and Methods below) of altered oceanic
106 crust (AOC) reveal two dominant dehydration stages along hot (1000 °C, 2.4 GPa) and cold (1000
107 °C, 3.3 GPa) subduction geothermal gradients (Fig. 1). The dehydration of chlorite and talc occurs
108 at temperatures (T) T < 575 °C with removal of ~20% of the total water contained in the hydrated
109 AOC (Figs. 1A, B and S1). The second stage occurs at fore-arc to sub-arc depths of 60–80 km for
110 warm subduction, and of 80–120 km for cold subduction. During this stage, ~75% of the initial water
111 contained in the AOC is released through dehydration of epidote, lawsonite, pumpellyite, and
112 stilpnomelane. Lawsonite and muscovite are predicted to carry the remaining ~5% of water in the
113 AOC to the deep mantle (> 120 km) in the cold subduction regime (Fig. 1B).

114 Our model predicts that about 60% and 90% of the initial sulfur in AOC is released from hot
115 and cold subducting slabs, respectively, during the second stage of dehydration (Figs. S1A and B).
116 Aqueous sulfur speciation evolves along the hot geotherm, transforming from dominantly reduced
117 (HS⁻ and H₂S) in the first dehydration stage to dominantly oxidized (HSO₄⁻, SO₄²⁻, KSO₄⁻, HSO₃⁻
118 and SO₂) during the second dehydration stage (Fig. 1C). In contrast, fluid speciation along the cold
119 geotherm is always dominated by sulfate with only minor H₂S, HS⁻ and SO₂ (Fig. 1D). For both hot
120 and cold subduction geotherms, the majority of the S is released to the aqueous fluid when pyrite
121 (S⁻) is oxidized to anhydrite (S⁶⁺) in the 475–600 °C range (Figs. 1 and S2). Our model predicts an
122 increase in the Fe³⁺/ΣFe ratio of garnet and decrease in clinopyroxene and the bulk rock system,
123 over the interval of pyrite oxidation to anhydrite, both for cold and hot subduction scenarios (Figs.
124 S1 and S2).

125 ***Oxidative capacity of slab-derived fluid***

126 To evaluate the metasomatic effects induced by slab-derived fluids in hot and cold subduction
127 zones, we calculated the change in oxygen fugacity (fO₂) caused by the infiltration of fluids
128 containing different S⁶⁺ concentrations (Fig. 2) into depleted mantle peridotite. For both hot and cold
129 subduction geotherms, the interaction of mantle rocks with a fluid typically containing 1 to 2 wt.%
130 S⁶⁺ increases the mantle fO₂ by at least two log units at plausible fluid/rock mass ratios (R) of 0.02
131 to 0.05 (Figs. 2A and B top curves). In contrast, in both regimes, only a weak increase in fO₂ (0.2-

132 0.5 log units) can be achieved by sulfur-poor (0.01-0.02 wt.% S) fluids and only at higher fluid/rock
133 ratios ($R > 0.2$) (Figs. 2A and B, bottom curves). This difference demonstrates the importance of
134 sulfur in the mantle oxidation process. Our model predicts that the mantle oxygen fugacity steeply
135 increases during the initial infiltration of the S^{6+} -bearing fluid. With further fluid infiltration, the
136 increase in fO_2 decreases (Figs. 2A and B). A similar pattern is displayed in the $Fe^{3+}/\Sigma Fe$ ratio of
137 garnet and pyroxene and X_{Mg} ($Mg/(Mg+Fe)$) values of olivine (Fig. S3). These results demonstrate
138 that the concentration of sulfate of the fluid plays a major role in the oxidation of the mantle wedge.
139 In addition, the fluid infiltration model (see Materials and Methods below) predicts that pyrrhotite
140 and pyrite are the dominant sulfide minerals for low to moderate degrees of metasomatism (i.e. low
141 fluid/rock ratios, $R < 0.01$). With increasing fluid/rock ratio, Py + Anh and Pyh + Anh become the
142 stable S-bearing mineral assemblages. The transition from Py + Anh to Pyh + Anh occurs at ~930
143 °C and ~1050 °C for hot and cold subduction models, respectively (Figs. 3C and D).

144 **Sulfur and gold abundances and chemical speciation in fluid reacted with mantle wedge**

145 The concentrations of sulfur species in slab-derived fluids after reaction with depleted mantle
146 peridotite were computed for temperature of 1000 °C and pressures of 2.4 and 3.3 GPa (Figs. 3, S4
147 and S5). At 2.4 GPa, in the presence of Py, Pyh and Anh, elevated concentrations of sulfate and
148 sulfite (HSO_4^- , SO_4^{2-} , HSO_3^- , SO_2) persist over a wide range of temperature (Figs. S4C–F). At low
149 fluid/rock mass ratios ($R < 0.01$), H_2S is the dominant aqueous sulfur species but the high
150 concentrations of HS^- in the reacted aqueous fluid occur only at 800–900 °C, as pH changes
151 toward more alkaline values (Figs. S4A and B). The highest concentrations of trisulfur radical ion
152 S_3^- in the reacted fluid occur at 700–1100 °C (Fig. 3A). Compared to H_2S and HS^- , S_3^- is more
153 abundant at higher fO_2 conditions, and accounts for $\geq 50\%$ of the total sulfur at fO_2 between
154 $\Delta FMQ+0.5$ and $\Delta FMQ+1.5$ (Figs. 2C and 3A). At 3.3 GPa, higher concentrations of HSO_4^- , HSO_3^-
155 and SO_2 are predicted over a wide range of temperatures and fluid/rock ratios (Figs. S5C–F).
156 Significant concentrations of H_2S and HS^- are restricted to areas of low fluid-rock ratios and to low
157 temperatures (< 900 °C) for HS^- (Figs. S5A and B). At R values between 0.002 and 0.02
158 (corresponding to fO_2 from $\Delta FMQ-0.5$ to $\Delta FMQ+1.5$), S_3^- is the dominant aqueous sulfur species
159 accounting for 50–90% of the total sulfur in the fluid (Fig. 3B). In both models, the abundance of S_3^-
160 is a strong function of fO_2 and the concentrations of S_3^- are one to three orders of magnitude higher
161 than those of HS^- at redox conditions, thus permitting sulfide-sulfate coexistence. Such
162 concentrations are expected to favor the formation of gold complexes with the S_3^- ligand.

163 To support this conclusion, we calculated the speciation and solubility of gold in a metamorphic
164 fluid (containing 3 wt.% S and 5 wt.% NaCl) typical of subduction zones at 600 °C and 1.5 GPa
165 (Figs. 3C and D). These calculations show that while $Au(HS)_2^-$ is the dominant gold complex below
166 FMQ redox conditions, $Au(HS)S_3^-$ becomes the dominant gold carrier at higher oxygen fugacity,
167 followed by $AuCl_2^-$ at highly oxidizing conditions ($> \Delta FMQ+3$) (Fig. 3C). The highest abundance of
168 $Au(HS)S_3^-$ occurs at redox conditions of the pyrite-pyrrhotite-magnetite buffer ($\sim \Delta FMQ+1$), when
169 the gold solubility is 2 ppm (Fig. 3C). In addition to redox conditions, the sulfur-content of the fluid is
170 an important parameter affecting Au solubility. At 600 °C, 1.5 GPa and redox conditions of
171 $H_2S:SO_2=1:1$, the concentration of $Au(HS)S_3^-$ complex is strongly enhanced in sulfur-rich (> 1 wt.%
172 S) fluids (Fig. 3D). Our calculations show that $Au(HS)S_3^-$ remains the major gold complex in sulfur-
173 rich solutions at 700 °C and 800 °C, in which Au solubility attains 100–300 ppb (Fig. S6). Gold
174 solubility and aqueous speciation are also functions of the fluid alkalinity (here defined as $\Delta pH =$
175 $pH-pH_n$, where pH_n is the pH value of the water neutrality point). At more acidic pH ($\Delta pH < -1$),
176 $AuCl_2^-$ becomes more important, but its abundance largely decreases with increasing pH (Fig. S7).
177 In contrast, $Au(HS)S_3^-$ and $Au(HS)_2^-$ complexes may transport ~2 ppm Au in the aqueous fluid at
178 neutral to alkaline conditions of ΔpH 0.0 to 2.5, which are typical of slab-derived fluids in equilibrium
179 with mantle peridotite (Fig. S7 and Supplementary Text). In summary, these mantle-wedge fluids
180 are expected to mobilize and concentrate large amounts of Au by forming abundant $Au(HS)S_3^-$
181 during mantle metasomatism.

Efficiency of gold extraction from oxidized hydrous mantle by partial melting

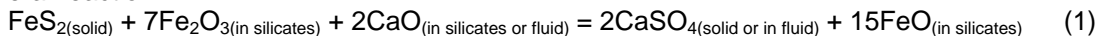
We estimated the gold extraction efficiency from a fertile mantle (containing 3.5 ppb Au and 600 ppm S) by modeling fluid-present batch melting at oxygen fugacities of $\Delta\text{FMQ}-1.0$ (reducing) and $\Delta\text{FMQ}+1.5$ (moderately oxidizing), respectively (Figs. 4, S8 and S9). Two scenarios were simulated: i) low-temperature melting (1100 °C, 1.5 GPa) with large fractions of monosulfide solid solution (MSS) and ii) high-temperature melting (1300 °C, 1.5 GPa) in the presence of sulfide liquid (SL). Both scenarios indicate that the consumption of mantle sulfide is favored by moderately oxidizing conditions. At $f\text{O}_2$ of $\Delta\text{FMQ}+1.5$, the silicate melt contains all Au and S for a melt degree (F) of $< 7.5\%$, due to the exhaustion of sulfide (Figs. 4B and D). At $f\text{O}_2$ of $\Delta\text{FMQ}-1.0$, only a small fraction of mantle Au is released into the silicate melt at a high degree of partial melting (up to 15%, Figs. 4A and C). Results for fluid-present melting models demonstrate that the coexistence of aqueous fluid and silicate melt is far more favorable for extraction of Au and S from mantle than in the absence of a fluid phase (Fig. 4). As shown in Figs. 4A and B, with only 1% partial melting, ~70% of Au in the mantle can be extracted in the presence of 0.3 wt.% fluid, with concentrations of 8 ppb Au in the water-saturated melt and 800 ppb Au in the coexisting fluid. With only 5.5% melting at $f\text{O}_2$ of $\Delta\text{FMQ}+1.5$ and in the presence of 0.2 wt.% fluid, mantle sulfide becomes exhausted (Figs. 4B and D). Thus, our models reveal that the stability of sulfide liquid is greatly diminished when the fluid phase appears. This fluid phase has the ability to transport ~60 times more Au than a silicate melt at mantle-wedge conditions of $\Delta\text{FMQ}+1.5$, 5 % melting fraction and only 0.2 wt.% aqueous fluid in the system.

Discussion

Controls on sulfur mass transfer at the slab-mantle interface

Previous thermodynamic modelling (14, 22, 23) has shown that slab devolatilization releases fluids in which sulfur could be present as $\text{CaSO}_4^0(\text{aq})$, SO_4^{2-} , HSO_4^- , HSO_3^- , SO_2 , H_2S , and HS^- . However, these ignored the trisulfur radical ion, S_3^- , that becomes increasingly abundant at elevated temperatures and pressures. Our study reveals that S_3^- is the dominant reduced species in fluids across a wide range of redox conditions after reaction with overlying mantle (Fig. 3). Figure 1 shows that the concentrations of sulfate and sulfite (e.g., SO_4^{2-} , HSO_4^- , HSO_3^-) in the fluid sharply increase, by one to three orders of magnitude, before reaching a plateau when pyrite is oxidized to anhydrite along both hot and cold subduction geotherms. The results presented here show that a maximum flux of oxidized fluid will be generated from AOC at 60–80 km and 80–120 km for hot and cold subduction zones, respectively. These predictions are similar to conditions at the depth of arc-magma formation. Results from the mantle infiltration model indicate that fluids released at sub-arc depth are capable of oxidizing the overlying mantle to $\Delta\text{FMQ}+2$ to 3, whereas fluids from fore-arc depths cannot increase mantle $f\text{O}_2$ values to more than $\Delta\text{FMQ}+1$ (Fig. 2). The higher oxidation state of sub-arc mantle is also consistent with the higher bulk-rock $\text{Fe}^{3+}/\Sigma\text{Fe}$ ratios of magmatic rocks (0.18–0.32) at volcanic arcs relative to those in back-arc, mid-ocean ridge, and fore-arc settings (6). Our predictions also fall in the $f\text{O}_2$ range of metasomatized mantle inferred from mantle xenoliths and arc magmas (9, 11).

As shown in Figs. 1 and S2, increasing temperature during prograde metamorphism of the subducting slab results in the oxidation of pyrite to anhydrite and the breakdown of hydrous minerals including epidote, chlorite and lawsonite. This process results in the growth of garnet at ~550 °C, a decrease of the $\text{Fe}^{3+}/\Sigma\text{Fe}$ ratio of clinopyroxene, and an increase in garnet with increasing temperature (Figs. S2C–H). The total Fe^{3+} content of the residual solid decreases by ~0.2 mol/kg rock over the temperature range within which pyrite is oxidized to anhydrite (Figs. S1C and D). From the sulfur loss curves and mineral modal abundances, ~0.03 mol/kg rock S^- (i.e. total initial sulfur content in model) is oxidized to S^{6+} when pyrite transforms to anhydrite (Figs. 1 and S1). Consequently, mass balance calculations indicate that this redox process is consistent with the general reaction:



Our model suggests that the oxidation of S during the thermally-induced breakdown of pyrite is

233 balanced by reduction of Fe³⁺ in bulk rock rather than reduction of CO₂ as previously proposed (14).
 234 Indeed, the bulk rock is the greatest reservoir of iron, including Fe³⁺, which is much greater than
 235 possible CO₂ input. The results indicate that the production of sulfate in the slab is a function of the
 236 Fe³⁺ content of the protolith. It follows that the transfer of sulfate to the slab-derived fluid will leave a
 237 reduced residual mineral assemblage in the subducting oceanic crust. This conclusion is consistent
 238 with natural observations, such that the increase of core to rim δ⁵⁶Fe values of garnet in garnet-
 239 epidote blueschist from the Sifnos subduction zone, Greece, which was attributed to the loss of
 240 oxidizing fluids during devolatilization of the subducting slab (10). Previous thermodynamic studies
 241 concluded that the transformation of pyrite to pyrrhotite dominates the release of sulfur from the
 242 subducted slab (23). Instead, our results suggest that the oxidation of pyrite to soluble sulfate
 243 during the blueschist to eclogite transition is responsible for introducing the major fraction of
 244 oxidized sulfur from the subducted slab into the sub-arc mantle.

245 The mantle oxidation model presented here predicts a positive correlation between the *f*O₂ of
 246 mantle and the increase of Fe³⁺/ΣFe ratios in pyroxene and garnet with the continuous infiltration of
 247 a S⁶⁺-bearing slab-derived fluid (Figs. 2 and S3). The consumption of Fe²⁺ is manifested by an
 248 increase in the modal abundances of orthopyroxene at the expense of olivine and clinopyroxene
 249 and an increase in the X_{Mg} value of olivine (Figs. S3A and B). Additionally, oxidized sulfur species
 250 (HSO₄⁻, SO₄²⁻, HSO₃⁻) in the infiltrating slab-derived fluid are reduced to HS⁻, H₂S, and S₃⁻ as the
 251 fluid is reacting with the mantle rock (Figs. 3, S4 and S5). These sulfate reduction reactions are
 252 consistent with a decrease in *f*O₂ values of slab-derived fluids after interaction with depleted mantle,
 253 for instance decreasing from ΔFMQ+5 to ΔFMQ+3 at sub-arc depths (Fig. 5A). We therefore
 254 propose that the following schematic reactions illustrating the control of sulfur and iron redox state
 255 in the mantle wedge:



259 Our model predicts that fluid-altered clinopyroxene and orthopyroxene in the mantle wedge will
 260 have Fe³⁺/ΣFe ratios of 0.30–0.45 and 0.10–0.20, respectively (Figs. S3C and D). These ratios
 261 broadly agree with analyzed values of 0.48–0.51 and 0.10–0.15 in fluid-altered metasomatic mantle
 262 peridotite from the Sulu orogeny in China (24), for clinopyroxene and orthopyroxene, respectively.
 263 Furthermore, increase of Fe³⁺/ΣFe values in metasomatized garnet is consistent with values for
 264 peridotite samples of the sub-arc mantle from Bardane in Norway (13). These observations
 265 collectively indicate that the oxidized state of the mantle wedge is caused by S⁶⁺-bearing slab-
 266 derived fluid metasomatism that results in the oxidation of Fe²⁺ in the silicate minerals, dissolution of
 267 sulfide minerals, and generation of reduced sulfur Au-complexing ligands such as H₂S (HS⁻) and
 268 S₃⁻ (Fig. 5).

269 ***Enhanced mobility and enrichment of gold in mantle wedge***

270 Mantle wedge metasomatized by slab-derived fluid and melts generally results in enrichment in
 271 metals (e.g., up to hundreds ppb Au and thousands ppm Te) and elevated oxygen fugacity
 272 (>ΔFMQ+1) (25, 26). However, the causes of metal enrichment during mantle oxidation process
 273 were poorly understood. Recent experimental studies imply that slab melts carry no more than ¼ of
 274 the Au from the downgoing lithosphere to the overlying mantle wedge. These data are corroborated
 275 by the low gold abundances (< 1ppb) in primitive melts from subduction-related eclogite (27, 28).
 276 Although some studies have inferred Au loss into devolatilization-induced fluids by prograde sulfide
 277 breakdown during slab subduction (29, 30), this gold input cannot explain the elevated Au
 278 abundance of the overall metasomatic mantle (31). We posit an alternative model in which the
 279 mobilization and redistribution of mantle Au plays a first-order control on the formation of auriferous
 280 metasomatized mantle by locally enhancing gold fertility of mantle lithosphere. Naturalistic support
 281 for this model comes from numerous reports of gold-rich lithospheric mantle in the Ivrea Zone, Italy
 282 (25), the Deseado Massif, Argentina (32), and at Tallante, southern Spain (33). In these settings,
 283 melt- or fluid- metasomatized mantle peridotite and pyroxenite have 10–100 times more Au than
 284 pristine mantle and some samples even contain visible native gold particles.

285 A statistical analysis of mantle peridotites (34) concluded that the Au concentrations gradually

286 increase with the evolution from deep garnet-bearing peridotite (0.5–1.5 ppb, max 3 ppb) to shallow
287 plagioclase-bearing peridotite (2–4 ppb, max 15 ppb). The Au abundances exhibit positive
288 correlations with the concentrations of incompatible elements in some mantle xenoliths (35). These
289 data collectively indicate upward mobilization of Au by aqueous fluids or hydrous melts, but the
290 abilities of fluid and melt to carry Au have not been quantified. Our numerical results show that the
291 S-bearing fluids can carry hundreds to thousands ppb of gold as the $\text{Au}(\text{HS})\text{S}_3^-$ complex across a
292 wide $f\text{O}_2$ (FMQ to $\Delta\text{FMQ}+2$) and pH ($\Delta\text{pH} = 0.0\text{--}2.5$) due to generation of abundant S_3^- in slab-
293 derived fluids upon reaction with depleted mantle (Figs. 3, S6 and S7). This enhanced transport
294 capacity provides an explanation for the Au enrichment in oxidized metasomatized mantle (Fig. 5B).
295 The consumption of these auriferous fluids during ascent through the mantle by hydration reactions
296 would form a mantle source locally enriched in Au and volatile elements (C-O-H-S) (Fig. 5A). This
297 scenario explains why sulfides hosted in weakly metasomatized mantle xenoliths (free of secondary
298 alteration minerals) have higher gold abundances (2 ppm) in comparison to those (<0.5 ppm)
299 hosted in strongly metasomatized rocks with secondary amphibole and apatite, such as in
300 Spitsbergen island, Norway (36). Alternatively, the Au-rich fluids produced by subduction-modified
301 mantle may directly contribute to the formation of gold deposits hosted in island arc zones, such as
302 Ladolam Au deposit, Papua New Guinea (37), and volcanogenic massive sulfide gold deposit in
303 Kermadec Arc (38). Due to a thinner lithosphere in such zones, auriferous fluid would transport
304 abundant Au and volatiles away from residual mantle sources to domains of arc-melt generated. In
305 summary, oxidation controls the metal enrichment in the metasomatized mantle via enhanced
306 mobilization of Au in complex with the trisulfur radical ion in aqueous fluid under more oxidizing
307 conditions than those of pristine mantle (Fig. 5).

308 ***Facilitated metal extraction and formation of gold deposits***

309 Partial melting of metasomatized mantle is regarded as a key process for the formation of
310 porphyry Cu-Au-Mo and epithermal Au-Ag deposits (32, 39). Gold concentrations of primary mantle
311 melts depend on the oxidation state of their source, degree of partial melting, and gold partitioning
312 between the sulfide phases and silicate melts (18, 40, 41). Low-degree melting of oxidized mantle
313 has been invoked to explain the formation of Au-rich parental arc magmas. For instance, ~2.4%
314 partial melting can yield Siberian picrite that contains abnormally high concentrations of Au and
315 platinum-group elements at redox conditions of $\Delta\text{FMQ}+2$ (42). Furthermore, oxidized mantle
316 xenoliths (with $\Delta\text{FMQ}+1$ to $\Delta\text{FMQ}+2$) from Lake Bullen Merri in Australia record extensive sulfide
317 dissolution at very low degrees of partial melting, of ~2% (11). These data are consistent with our
318 modeling that suggests gold is preferentially enriched in moderately oxidized ($\sim\Delta\text{FMQ}+1.5$) and
319 hydrous melts (Figs. 4, S8 and S9). Gold partitioning between silicate melt and sulfide is another
320 factor influencing the Au concentration of magma. Previous experimental investigations
321 demonstrate that iron sulfide occurs as both MSS and SL in upper mantle at redox conditions close
322 to the sulfide-sulfate boundary (SSO, $\sim\Delta\text{FMQ}+1.5$), which is regarded as typical $f\text{O}_2$ conditions of
323 metasomatized mantle (9, 43). The high Au partition coefficients (> 1000) between SL and mantle
324 melts result in most gold being retained in the residual SL until its complete resorption at higher $f\text{O}_2$
325 (44, 45). Consequently, increasing $f\text{O}_2$ to higher than SSO levels by the addition of slab-derived
326 Fe^{3+} was thought to account for the formation of Au-rich melts at high-temperature melting in the
327 presence of sulfide liquid (18). However, our modeling quantitatively shows that the aqueous fluid
328 only carries a few hundred ppm Fe^{3+} at sub-arc depths (Fig. S10). Whereas slab-derived hydrous
329 melts may carry 1–2 orders of magnitude more ferric iron than aqueous fluid, they are generally
330 expected to occur at slab depths greater than 100 km (4, 18, 46). Therefore, elevating $f\text{O}_2$ by
331 adding slab-derived Fe^{3+} is unlikely to be a prevalent process that promotes the release of Au from
332 sulfide liquid. Rather, fluid-present mantle melting can scavenge gold more efficiently from mantle
333 sulfide liquid under moderately oxidizing conditions resulting in readily exhaustion of mantle sulfides
334 even at small degrees of partial melting (Figs. 4 and S9). Note that the coexistence of aqueous fluid
335 and peridotite melt at our T-P conditions is consistent with experimentally established phase
336 diagrams (47), showing fluid-melt immiscibility up to at least 3.8 GPa and 1000–1100 °C. The fluid-
337 present partial melting of mantle wedge is also documented by the coexisting fluid and silicate melt
338 inclusions trapped in mantle peridotite xenoliths from western Hungary (48). These findings provide

339 a novel mechanism for generating Au-rich melts under redox conditions close to the coexistence of
340 sulfide and sulfate. Our predictions are supported by natural examples such as basanitic magmas
341 from Hawaii (formed at fO_2 of $\Delta FMQ+0.8$) with Au concentrations up to 36 ppb (49), volatile-rich
342 lamprophyres from Scotland, southern Africa, and the Yilgarn, Australia as the products of low-
343 degree mantle melting having 100–1000 times higher Au abundances than other ‘common’ igneous
344 rocks (50).

345 Gold grades of porphyry copper(-gold) deposits vary over three orders of magnitude, from
346 ~0.001 to 1 ppm Au. High Au-tonnage deposits show 10–100 times higher average gold grades
347 than those with high Cu tonnage (Fig. S11). Melt inclusion data from igneous rocks that were the
348 source of ore fluids for porphyry Cu(-Au) deposits in the Maricunga Belt, Chile, indicate that the Au
349 concentrations of magmas were as much as three orders of magnitude higher than those reported
350 for magmas of Cu-rich porphyry deposits (51). These differences in Au grades are likely due to the
351 sulfur control on the deep source of metals and variation of partial melting mechanism. Our
352 calculations suggest that the aqueous fluid acts as an extremely effective agent to transport and
353 concentrate Au within the metasomatic mantle wedge. Mass balance calculations further indicate
354 that 20–80% of the original mantle Au are released at < 2% hydrous low-temperature (1100 °C)
355 partial melting in the stability field of MSS (Figs. 4A and B). Therefore, the high fluid flux favors the
356 gold enrichment into shallow mantle lithosphere by upward mobilization at active continental
357 margins characterized by a thick lithosphere and cold mantle wedge, which, in turn leads to arc
358 magmas derived from deep mantle becoming Au depleted. Furthermore, this enriched mantle can
359 be stored hundreds of million years before a later tectonic melting event, as likely in the case of
360 Lake Bullen Merri in Australia (11), and is therefore an important metal source for Au deposits
361 formed in post-subduction settings (52). In contrast, in island arc subduction zone, high mantle
362 temperature of > 1300 °C stabilizes the sulfide liquid, thereby resulting in > 80% of the initial Au
363 retained in mantle source rather than extracted by silicate melt until exhaustion of sulfide (Figs. 4C
364 and D). In these settings, according to our modeling fluid-assisted high-temperature melting of
365 metasomatic mantle favors the generation of Au-enriched primary melts (Figs. 4 and S9), as
366 suggested for the high-Au arc magmas (> 8 ppb) from Kermadec arc (53). Our findings thus offer
367 another new perspective for understanding the variation of Au-grade in porphyry deposits located in
368 thick or thin lithosphere zones (54).

369 Previous metamorphic devolatilization scenarios explain the formation of Phanerozoic orogenic
370 gold from a metasomatized mantle source (e.g., in Jiaodong Peninsula in China (55, 56) and in
371 northwestern Mexico (57)). These scenarios postulate that gold and sulfur are released into the
372 fluids through breakdown of pyrite to pyrrhotite, conditions at which H_2S and HS^- are postulated to
373 be the ligands transporting gold (58). In contrast, our numerical modeling reveals that the sulfide-
374 sulfate transition provides the most favorable window for sulfur release under conditions typical of
375 the metasomatized mantle. At such conditions, the high abundance of S_3^- enables at least 10 to
376 100 times more efficient mobilization of gold by S-rich fluids than any common ligand such as H_2S ,
377 HS^- or Cl^- (Figs. 3C and D). The breakdown of S_3^- at lower temperatures and pressures would
378 trigger efficient and focused Au precipitation in upper levels of the crust where most deposits form
379 (20, 59). Consequently, S_3^- may be a key factor ensuring the generation of an auriferous fluid in
380 metasomatized mantle lithosphere (Fig. 5). In conclusion, our results demonstrate that mantle
381 oxidation by S-bearing aqueous fluids is the key trigger mechanism for Au enrichment and release
382 within mantle wedge, providing both the necessary source and transport conditions for the
383 formation of gold-rich porphyry-epithermal and orogenic gold systems. Additional work on both
384 chemical and physical reactive transport models will be a priority to advance our understanding of
385 metal enrichment and the transfer of the fluid-saturated silicate melt through the mantle wedge and
386 its ascent to shallower crust levels in subduction zones.

387 **Materials and Methods**

388 ***System compositions and redox budgets***

389 Bulk rock compositions chosen to model the altered oceanic crust and depleted mantle
390 peridotite systems were modified from refs. (60) and (61) (Table S1 and S2). Different water

391 contents were chosen for the hot and cold subduction zone regimes to enable H₂O saturation at the
392 first P-T point, with contents of 4.7 and 7.6 wt.%, respectively. The redox budget (RB) is a critical
393 variable for quantifying the potential redox capacity of a rock-fluid system, which is defined as:

$$RB = \sum n_j v_j$$

394 where v_j represents the number of electrons per mole required to convert a redox-sensitive element
395 from a reduced state to the reference oxidation state, and n_j is the number of moles of the element
396 per 1 kg of fluid-rock system. Here we only define the redox budget of initial solid rock, as the
397 remainder can be calculated using the thermodynamic modeling software. Iron, carbon and sulfur
398 were considered to be the major redox-sensitive elements in our model. For depleted mantle
399 peridotite, the initial oxidation states of iron, carbon and sulfur were set as Fe²⁺, C⁰, and S²⁻, with
400 minor Fe³⁺ corresponding to an Fe³⁺/ΣFe ratio of 0.031 (15). In view of the limited contents of CO₂
401 (50 ppm) in the depleted mantle, their influence on the model results is negligible. Compared with
402 the juvenile oceanic crust, the altered oceanic crust is characterized by higher Fe³⁺/ΣFe values,
403 which were adopted as 0.51. The redox states of sulfur were adopted to be S⁻ in pyrite and S⁶⁺ in
404 anhydrite with concentrations of 700 ppm and 364 ppm S, respectively. The composition of the
405 modeled rocks is listed in Table S1.

406 **Phase equilibrium modeling**

407 Our modeling includes a devolatilization model of AOC along hot and cold subduction paths,
408 and a mantle infiltration model. The geothermal models of Central Honshu and Central Cascadia
409 subduction zones were chosen to represent, respectively, the cold and hot thermal regime of the
410 subducting slab (62). The devolatilization model was calculated along the top-of-slab P-T paths in
411 both geothermal regimes, and each geotherm was discretized into 671 P-T points from 0.50 GPa to
412 7.20 GPa with a step of 0.01 GPa. When simulating the devolatilization processes of the subducting
413 slab, the fluid produced at a given P-T point was separated from the bulk rock. To quantify the
414 relative oxidation capacity of the slab-derived fluid, two methods were employed in simulating
415 mantle infiltration processes: a titration scenario and a mixing scenario. In the former, fluid
416 compositions were extracted from three different slab depths (see Fig. 1), then equilibrated with
417 model mantle peridotite at 3.3 GPa, 1000 °C and 2.4 GPa, 1000 °C for cold and hot subduction
418 models, respectively. The extracted fluid composition was normalized to 2 moles of hydrogen (H),
419 which is roughly equivalent to 1 mole of H₂O-dominated fluid, corresponding to 18 g (Table S3). We
420 divided 12 moles of such a fluid into 120 equal portions of 0.1 mole, and added one portion into 1
421 kg of model peridotite at each subsequent step. In the mixing scenario, 1 mole of fluid (normalized
422 to 2 moles of H) released at sub-arc depth as an endmember was reacted with 1 kg of mantle
423 peridotite as the other endmember at different fluid/rock mass ratios, from 700 °C to 1100 °C. The
424 compositions of 1 mol fluid and 1 kg rock are expressed here as elemental concentrations in
425 numbers of moles (Table S2 and S3). The fluid-rock ratio increases nonlinearly due to the following
426 dependence between the masses of reacting fluid and rock in a mixing model:

$$R = \frac{m_{fluid} \times X_{fluid}}{m_{rock} \times (1 - X_{fluid})}$$

427 where R is fluid-rock mass ratio of the system at a specific X_{fluid} value, and m_{fluid} and m_{rock} represent
428 initial masses of fluid (18 g) and mantle peridotite (1000 g), respectively. The X_{fluid} is an independent
429 variable with values between 0 and 1. For example, an X_{fluid} value of 0.9 on this scale corresponds
430 to a mass fluid/rock ratio of 0.16. All calculations were executed by Gibbs energy minimization in
431 Perple_X 7.0.11 (14, 63), using so called “lagged speciation” method of Perple_X to compute the
432 concentrations of aqueous species (14). Both for the devolatilization and mantle oxidation models,
433 the fluid was considered as a H₂O-CO₂ binary solution (14). Thermodynamic data for aqueous
434 species (except S₃⁻) are taken from the SUCRT92 database (64) complemented by the Deep Earth
435 Water model for Ca, Mg, Fe, Al and Si species (65) and those for minerals from the revised Holland
436 and Powell mineral database (66). The thermodynamic parameters of S₃⁻ are taken from ref. (59)
437 based on direct experimental measurements and revised Helgeson-Kirkham-Flowers (HKF)
438 equation of state compatible with the DEW model. Organic species were excluded from the
439 calculations. Amphibole, biotite, chlorite, clinopyroxene, dolomite, epidote, feldspar, garnet,

440 magnesite, muscovite, pumpellyite, pyrrhotite, olivine, orthopyroxene, stilpnomelane, and talc were
 441 treated as solid solutions. All other minerals were treated as pure phase compounds, including
 442 albite, anhydrite, coesite, kyanite, lawsonite, pyrite, quartz, and stilbite. For more details on solid
 443 solution models and fluid equations of state see [Tables S4 and S5](#).

444 **Modeling of Au speciation and solubility in the fluid phase**

445 Gold speciation and solubility in H₂O-NaCl-S aqueous fluids at 1.5 GPa, 600 °C, which are
 446 typical dehydration conditions of AOC and serpentinized oceanic mantle, were modeled to explore
 447 the geochemical behavior of Au during mantle metasomatism. The main fluid constituents include 6
 448 wt.% NaCl (67), 3 wt.% S (68) and an excess of native gold. The fluid pH was buffered at a value of
 449 about 5 by using the olivine-pyroxene-garnet mantle mineral assemblage, which corresponds to
 450 slightly alkaline conditions relative to the neutrality point of pure water ($\Delta\text{pH}=1.5$ to 2.5, see
 451 Supplementary Materials). The thermodynamic properties of minerals and major fluid constituents,
 452 including most sulfur species, are from the updated Holland and Powell (69) and SUPCRT
 453 databases (64), respectively. The HKF equation of state parameters for the S₃⁻ ion were adopted
 454 from ref. (59). The complexes Au(HS)₂⁻, AuCl₂⁻, and Au(HS)S₃⁻, for which robust thermodynamic
 455 data were constrained over a wide P-T range (20, 70, 71), were considered in the modeling.
 456 Species such as AuHS⁰, AuHS(H₂S)₃⁰, AuOH⁰, AuCl⁰, and Au(OH)₂⁻ were ignored because of the
 457 large uncertainties associated with their identity and stability at elevated temperatures and
 458 inconsistencies in their published thermodynamic parameters. Sources of the thermodynamic
 459 properties of Au-HS-Cl-S₃⁻ species are reported in [Table S5](#). These datasets arise from the large
 460 amount of experimental work described by the HKF equation of state, which enables plausible
 461 extrapolations to the high temperatures and pressures of our system. Calculations were conducted
 462 using the HCh package and modified and updated Unitherm database (72).

463 **Estimation of gold extraction during hydrous mantle melting**

464 The available partial melting models disregard the effects of an aqueous fluid phase on the
 465 element distribution. In this study, we applied mass balance relationships to quantify, for the first
 466 time, the Au contents released into the fluid and silicate melt during partial melting of mantle. We
 467 calculated a batch melting process at a given free aqueous fluid phase fraction varying from 0.1 to
 468 0.3 wt.% of the melt-fluid-rock system. Mantle Au is stored almost exclusively by iron sulfide solid or
 469 liquid with negligible Au fractions in other silicate minerals or as a metallic gold particle. Therefore,
 470 the total Au content in a closed system at equilibrium is given by the following equation:

$$M_{\text{Au}} = C_{\text{Au}}^{\text{sulf}} \times m_{\text{sulfide}} + C_{\text{Au}}^{\text{fluid}} \times m_{\text{fluid}} + C_{\text{Au}}^{\text{melt}} \times m_{\text{melt}}$$

471 where M_{Au} is the total Au content per unit mass of mantle rock, $m_{(j)}$ and $C_{\text{Au}}^{(j)}$ are the mass fraction
 472 and Au concentration of the iron sulfide phase, aqueous fluid phase and silicate melt phase,
 473 respectively. According to the gold partition coefficients of sulfide/melt ($D_{\text{Au}}^{\text{sulfide/melt}}$) and fluid/melt
 474 ($D_{\text{Au}}^{\text{fluid/melt}}$), the above equation can be re-arranged to express the Au concentration in silicate melt:

$$C_{\text{Au}}^{\text{melt}} = \frac{M_{\text{Au}}}{D_{\text{Au}}^{\text{sulfide/melt}} \times m_{\text{sulfide}} + D_{\text{Au}}^{\text{fluid/melt}} \times m_{\text{fluid}} + m_{\text{melt}}}$$

475 The Au concentrations in aqueous fluid and sulfide can thus be estimated by mass balance in
 476 close-system batch melting, which is given by:

$$C_{\text{Au}}^{\text{fluid}} = C_{\text{Au}}^{\text{melt}} \times D_{\text{Au}}^{\text{fluid/melt}}, \quad C_{\text{Au}}^{\text{sulfide}} = C_{\text{Au}}^{\text{melt}} \times D_{\text{Au}}^{\text{sulfide/melt}}$$

477 The mass fraction of melt, m_{melt} , depends on the melting degree, F, the mass fraction of residual
 478 sulfur in mantle rock at any given F value, and the fluid content:

$$M_{\text{S}}^{\text{rock}} = M_{\text{S}_t}^i - C_{\text{S}}^{\text{fluid}} \times m_{\text{fluid}} - C_{\text{S}}^{\text{melt}} \times F$$

479 where $M_{\text{S}}^{\text{rock}}$ and $M_{\text{S}_t}^i$ represent the residual and initial sulfur content in mantle rock, $C_{\text{S}}^{\text{fluid}}$ and $C_{\text{S}}^{\text{melt}}$
 480 are sulfur concentrations that solubilities in aqueous fluid and mantle melts, which were determined
 481 by regression of the available experimental data ([Fig. S12](#)). Sulfide has long been known to occur
 482 as both monosulfide solid solution (MSS) and liquid (SL) phases at upper mantle temperature and
 483 pressure, and its phase state (solid or liquid) exerts a first-order control on Au partitioning during

484 mantle melting (42, 45). Available experimental data indicate that MSS and SL are stable,
485 respectively, at < 1200 °C and ≥ 1300 °C, at pressures of 1.5 GPa, corresponding to mantle partial
486 melting depths (43). Therefore, in our melting model, two scenarios, a high-temperature (1300 °C)
487 and a low-temperature (1100 °C) one, for hydrous mantle melting were simulated at two different
488 redox conditions, of ΔFMQ+1.5 and ΔFMQ−1.0. The initial Au concentration of metasomatized
489 mantle was assumed to be 3.5 ppb (34), and the sulfur concentration was chosen to be 600 ppm,
490 corresponding to 0.17 wt.% of monosulfide solid solution in the system (73). The partition
491 coefficients of Au between MSS or SL, and aqueous fluid and silicate melts are from the available
492 experimental data (44, 74) whose typical values for the conditions of our study were adopted as
493 $D_{Au}^{MSS/melt}$ of 200, $D_{Au}^{SL/melt}$ of 2200, and $D_{Au}^{fluid/melt}$ of 100. These data, both on sulfur solubility and Au
494 partitioning are from direct fluid-saturated melting experiments, thereby allowing gold extraction
495 from metasomatic mantle via hydrous melting to be estimated (see Supplementary Materials for
496 more details for model limitations and uncertainties).

497 Acknowledgments

498 KFQ and JD acknowledge Professor Richard Goldfarb and David Groves for their insights and
499 discussions on the theme of gold enrichment within metasomatic mantle throughout the years. KFQ
500 thanks the position of guest professor granted by Université de Toulouse III Paul Sabatier. This
501 work was supported by the High-performance Computing Platform of China University of
502 Geosciences Beijing. This research was financially supported by the National Natural Science
503 Foundation of China (42130801, 42261134535 and 42072087), the National Key Research
504 Program (2023YFF0804200 and 2023YFC2906900), the Frontiers Science Center for Deep-time
505 Digital Earth (2652023001), and the 111 Project of the Ministry of Science and Technology
506 (BP0719021), Shandong Provincial Bureau of Geology and Mineral Resources No.6 Geological
507 Brigade (LDKJ20240101). ACS acknowledges funding from the U.S. National Science Foundation
508 EAR Grants 2214119 and 2233425. GSP acknowledges funding from the Institut Carnot ISIFoR
509 (grant AsCOcrit) and the CNRS through the MITI interdisciplinary program “Conditions Extremes
510 2024” (grant ExtremeS). Lastly, we are grateful to Editors May R. Berenbaum, Huda Akil and Terry
511 Plank, and two anonymous reviewers whose constructive comments greatly improved the article.

512 References

- 513 1. J. J. Ague *et al.*, Slab-derived devolatilization fluids oxidized by subducted
514 metasedimentary rocks. *Nat. Geosci.* **15**, 320-326 (2022).
- 515 2. T. Kawamoto *et al.*, Mantle wedge infiltrated with saline fluids from dehydration and
516 decarbonation of subducting slab. *Proc. Nat. Acad. Sci.* **110**, 9663-9668 (2013).
- 517 3. W. Sun, R. J. Arculus, V. S. Kamenetsky, R. A. Binns, Release of gold-bearing fluids in
518 convergent margin magmas prompted by magnetite crystallization. *Nature* **431**, 975-978
519 (2004).
- 520 4. K. Mibe, T. Kawamoto, K. N. Matsukage, Y. Fei, S. Ono, Slab melting versus slab
521 dehydration in subduction-zone magmatism. *Proc. Nat. Acad. Sci.* **108**, 8177-8182 (2011).
- 522 5. T. Plank, C. E. Manning, Subducting carbon. *Nature* **574**, 343-352 (2019).
- 523 6. K. A. Kelley, E. Cottrell, Water and the oxidation state of subduction zone magmas. *Science*
524 **325**, 605-607 (2009).
- 525 7. J. C. M. D. Hoog, E. Clarke, K. Hattori, Mantle wedge olivine modifies slab-derived fluids:
526 Implications for fluid transport from slab to arc magma source. *Geology* **51**, 663-667 (2023).
- 527 8. P. Tollan, J. Hermann, Arc magmas oxidized by water dissociation and hydrogen
528 incorporation in orthopyroxene. *Nat. Geosci.* **12**, 667-671 (2019).
- 529 9. A. Bénard *et al.*, Oxidising agents in sub-arc mantle melts link slab devolatilisation and arc
530 magmas. *Nat. Commun.* **9**, 3500 (2018).
- 531 10. A. R. Gerrits *et al.*, Release of oxidizing fluids in subduction zones recorded by iron isotope
532 zonation in garnet. *Nat. Geosci.* **12**, 1029-1033 (2019).
- 533 11. A. Rielli *et al.*, Incipient metal and sulfur extraction during melting of metasomatised mantle.
534 *Earth Planet. Sci. Lett.* **599**, 117850 (2022).

- 535 12. M. J. Muth, P. J. Wallace, Slab-derived sulfate generates oxidized basaltic magmas in the
536 southern Cascade arc (California, USA). *Geology* **49**, 1177-1181 (2021).
- 537 13. A. Rielli *et al.*, Evidence of sub-arc mantle oxidation by sulphur and carbon. *Geochem.*
538 *Persp. Lett.* **3**, 124-132 (2017).
- 539 14. J. A. D. Connolly, M. E. Galvez, Electrolytic fluid speciation by Gibbs energy minimization
540 and implications for subduction zone mass transfer. *Earth Planet. Sci. Lett.* **501**, 90-102
541 (2018).
- 542 15. J. A. Padrón-Navarta, V. López Sánchez-Vizcaíno, M. D. Menzel, M. T. Gómez-Pugnaire,
543 C. J. Garrido, Mantle wedge oxidation from deserpentinization modulated by sediment-
544 derived fluids. *Nat. Geosci.* **16**, 268-275 (2023).
- 545 16. M. J. Muth, P. J. Wallace, Sulfur recycling in subduction zones and the oxygen fugacity of
546 mafic arc magmas. *Earth Planet. Sci. Lett.* **599**, 117836 (2022).
- 547 17. Z. Taracsák *et al.*, Sulfur from the subducted slab dominates the sulfur budget of the mantle
548 wedge under volcanic arcs. *Earth Planet. Sci. Lett.* **602**, 117948 (2023).
- 549 18. J. E. Mungall, Roasting the mantle: Slab melting and the genesis of major Au and Au-rich
550 Cu deposits. *Geology* **30**, 915-918 (2002).
- 551 19. R. E. Botcharnikov *et al.*, High gold concentrations in sulphide-bearing magma under
552 oxidizing conditions. *Nat. Geosci.* **4**, 112-115 (2011).
- 553 20. G. S. Pokrovski, N. N. Akinfiyev, A. Y. Borisova, A. V. Zotov, K. Kouzmanov, Gold speciation
554 and transport in geological fluids: insights from experiments and physical-chemical
555 modelling. *Geol. Soc. Lond. Spec. Publ.* **402**, 9-70 (2014).
- 556 21. G. S. Pokrovski, L. S. Dubrovinsky, The S_3^- ion is stable in geological fluids at elevated
557 temperatures and pressures. *Science* **331**, 1052-1054 (2011).
- 558 22. J. B. Walters, A. M. Cruz-Uribe, H. R. Marschall, Sulfur loss from subducted altered oceanic
559 crust and implications for mantle oxidation. *Geochem. Persp. Lett.* **13**, 36-41 (2020).
- 560 23. A. G. Tomkins, K. A. Evans, Separate zones of sulfate and sulfide release from subducted
561 mafic oceanic crust. *Earth Planet. Sci. Lett.* **428**, 73-83 (2015).
- 562 24. N. Malaspina, F. Langenhorst, P. Fumagalli, S. Tumiatei, S. Poli, Fe^{3+} distribution between
563 garnet and pyroxenes in mantle wedge carbonate-bearing garnet peridotites (Sulu, China)
564 and implications for their oxidation state. *Lithos* **146-147**, 11-17 (2012).
- 565 25. D. A. Holwell *et al.*, A metasomatized lithospheric mantle control on the metallogenic
566 signature of post-subduction magmatism. *Nat Commun* **10**, 3511 (2019).
- 567 26. K.-F. Qiu *et al.*, The role of an oxidized lithospheric mantle in gold mobilization. *Sci. Adv.*
568 **10**, eado6262.
- 569 27. Z. Zou *et al.*, Deep mantle cycle of chalcophile metals and sulfur in subducted oceanic
570 crust. *Geochim. Cosmochim. Acta* **370**, 15-28 (2024).
- 571 28. Y. Li *et al.*, An essential role for sulfur in sulfide-silicate melt partitioning of gold and
572 magmatic gold transport at subduction settings. *Earth Planet. Sci. Lett.* **528**, 115850 (2019).
- 573 29. S. Aulbach *et al.*, Siderophile and chalcophile elements in spinels, sulphides and native Ni
574 in strongly metasomatised xenoliths from the Bultfontein kimberlite (South Africa). *Lithos*
575 **380-381**, 105880 (2021).
- 576 30. J. B. Walters, A. M. Cruz-Uribe, H. R. Marschall, B. Boucher, The role of sulfides in the
577 chalcophile and siderophile element budget of the subducted oceanic crust. *Geochim.*
578 *Cosmochim. Acta* **304**, 191-215 (2021).
- 579 31. Z. Wang *et al.*, Metasomatized lithospheric mantle for Mesozoic giant gold deposits in the
580 North China craton. *Geology* **48**, 169-173 (2019).
- 581 32. S. Tassara *et al.*, Plume-subduction interaction forms large auriferous provinces. *Nat.*
582 *Commun.* **8**, 843 (2017).
- 583 33. J. M. González-Jiménez *et al.*, Mineralogy of the HSE in the subcontinental lithospheric
584 mantle —An interpretive review. *Lithos* **372-373**, 105681 (2020).
- 585 34. J. E. Saunders, N. J. Pearson, S. Y. O'Reilly, W. L. Griffin, Gold in the mantle: A global
586 assessment of abundance and redistribution processes. *Lithos* **322**, 376-391 (2018).
- 587 35. P. Kepezhinskas, M. J. Defant, E. Widom, Abundance and distribution of PGE and Au in
588 the island-arc mantle: implications for sub-arc metasomatism. *Lithos* **60**, 113-128 (2002).

- 589 36. J. E. Saunders, N. J. Pearson, S. Y. O'Reilly, W. L. Griffin, Sulfide metasomatism and the
590 mobility of gold in the lithospheric mantle. *Chem. Geol.* **410**, 149-161 (2015).
- 591 37. B. I. A. McInnes, J. S. McBride, N. J. Evans, D. D. Lambert, A. S. Andrew, Osmium Isotope
592 Constraints on Ore Metal Recycling in Subduction Zones. *Science* **286**, 512-516 (1999).
- 593 38. C. Timm, C. E. J. de Ronde, M. I. Leybourne, D. Layton-Matthews, I. J. Graham, Sources of
594 Chalcophile and Siderophile Elements in Kermadec Arc Lavas*. *Econ. Geol.* **107**, 1527-
595 1538 (2012).
- 596 39. A. C. Simon, E. M. Ripley, The role of magmatic sulfur in the formation of ore deposits. *Rev.*
597 *Mineral. Geochem.* **73**, 513-578 (2011).
- 598 40. J. P. Richards, Giant ore deposits formed by optimal alignments and combinations of
599 geological processes. *Nat. Geosci.* **6**, 911-916 (2013).
- 600 41. J. E. Mungall, J. J. Hanley, N. T. Arndt, A. Debecdelievre, Evidence from meimechites and
601 other low-degree mantle melts for redox controls on mantle-crust fractionation of platinum-
602 group elements. *Proc. Nat. Acad. Sci.* **103**, 12695-12700 (2006).
- 603 42. J. E. Mungall, D. R. A. Andrews, L. J. Cabri, P. J. Sylvester, M. Tubrett, Partitioning of Cu,
604 Ni, Au, and platinum-group elements between monosulfide solid solution and sulfide melt
605 under controlled oxygen and sulfur fugacities. *Geochim. Cosmochim. Acta* **69**, 4349-4360
606 (2005).
- 607 43. Z. Zhang, M. M. Hirschmann, Experimental constraints on mantle sulfide melting up to 8
608 GPa. *Am. Mineral.* **101**, 181-192 (2016).
- 609 44. R. E. Botcharnikov *et al.*, Behavior of gold in a magma at sulfide-sulfate transition:
610 Revisited. *Am. Mineral.* **98**, 1459-1464 (2013).
- 611 45. J. E. Mungall, J. M. Brenan, Partitioning of platinum-group elements and Au between
612 sulfide liquid and basalt and the origins of mantle-crust fractionation of the chalcophile
613 elements. *Geochim. Cosmochim. Acta* **125**, 265-289 (2014).
- 614 46. C. Tiraboschi *et al.*, Preferential mobilisation of oxidised iron by slab-derived hydrous
615 silicate melts. *Geochem. Persp. Lett.* **24**, 43-47 (2023).
- 616 47. K. Mibe *et al.*, Second critical endpoint in the peridotite-H₂O system. *Journal of*
617 *Geophysical Research: Solid Earth* **112** (2007).
- 618 48. K. Hidas *et al.*, Coexisting silicate melt inclusions and H₂O-bearing, CO₂-rich fluid
619 inclusions in mantle peridotite xenoliths from the Carpathian–Pannonian region (central
620 Hungary). *Chem. Geol.* **274**, 1-18 (2010).
- 621 49. T. W. Sisson, Native gold in a Hawaiian alkalic magma. *Econ. Geol.* **98**, 643-648 (2003).
- 622 50. N. M. S. Rock, D. I. Groves, Do lamprophyres carry gold as well as diamonds? *Nature* **332**,
623 253-255 (1988).
- 624 51. J. T. Ovalle, A. C. Simon, M. Schirra, Z. Zajacz ("Understanding the Genesis of Gold-rich
625 Porphyry Systems: A case of Study from the Dorado Porphyry Gold Deposit in the
626 Maricunga Belt, Northern Chile". pp V43A-04.
- 627 52. J. P. Richards, Postsubduction porphyry Cu-Au and epithermal Au deposits: Products of
628 remelting of subduction-modified lithosphere. *Geology* **37**, 247-250 (2009).
- 629 53. C. Timm *et al.*, Hydrous mantle melting controls gold enrichment in Kermadec arc magmas.
630 (2024).
- 631 54. J.-W. Park, I. H. Campbell, M. Chiaradia, H. Hao, C.-T. Lee, Crustal magmatic controls on
632 the formation of porphyry copper deposits. *Nature Reviews Earth & Environment* **2**, 542-
633 557 (2021).
- 634 55. K. F. Qiu *et al.*, Gold deposits of the Jiaodong Peninsula, eastern China. *SEG Spec. Publ*
635 **23**, 753-773 (2020).
- 636 56. J. Deng *et al.*, An integrated mineral system model for the gold deposits of the giant
637 Jiaodong province, eastern China. *Earth Sci. Rev.* **208**, 103274 (2020).
- 638 57. A. Izaguirre *et al.*, Tectonic framework for Late Cretaceous to Eocene quartz-gold vein
639 mineralization from the Caborca Orogenic Gold Belt in Northwestern Mexico. *Econ. Geol.*
640 **112**, 1509-1529 (2017).
- 641 58. D. I. Groves, L. Zhang, M. Santosh, Subduction, mantle metasomatism, and gold: A
642 dynamic and genetic conjunction. *GSA Bulletin* **132**, 1419-1426 (2019).

- 643 59. G. S. Pokrovski, J. Dubessy, Stability and abundance of the trisulfur radical ion S_3^- in
644 hydrothermal fluids. *Earth Planet. Sci. Lett.* **411**, 298-309 (2015).
- 645 60. K. A. Kelley, T. Plank, J. Ludden, H. Staudigel, Composition of altered oceanic crust at
646 ODP Sites 801 and 1149. *Geochem. Geophys. Geosyst.* **4**, 8910 (2003).
- 647 61. V. J. M. Salters, A. Stracke, Composition of the depleted mantle. *Geochem. Geophys.*
648 *Geosyst.* **5**, Q05B07 (2004).
- 649 62. E. M. Syracuse, P. E. van Keken, G. A. Abers, The global range of subduction zone thermal
650 models. *Phys. Earth Planet. Inter.* **183**, 73-90 (2010).
- 651 63. M. E. Galvez, J. A. D. Connolly, C. E. Manning, Implications for metal and volatile cycles
652 from the pH of subduction zone fluids. *Nature* **539**, 420-424 (2016).
- 653 64. J. W. Johnson, E. H. Oelkers, H. C. Helgeson, SUPCRT92: A software package for
654 calculating the standard molal thermodynamic properties of minerals, gases, aqueous
655 species, and reactions from 1 to 5000 bar and 0 to 1000°C. *Comput. Geosci.* **18**, 899-947
656 (1992).
- 657 65. F. Huang, D. A. Sverjensky, Extended Deep Earth Water Model for predicting major
658 element mantle metasomatism. *Geochim. Cosmochim. Acta* **254**, 192-230 (2019).
- 659 66. T. J. B. Holland, R. Powell, An improved and extended internally consistent thermodynamic
660 dataset for phases of petrological interest, involving a new equation of state for solids. *J.*
661 *Metamorph. Geol.* **29**, 333-383 (2011).
- 662 67. Y. Huang, T. Nakatani, M. Nakamura, C. McCammon, Saline aqueous fluid circulation in
663 mantle wedge inferred from olivine wetting properties. *Nat. Commun.* **10**, 5557 (2019).
- 664 68. S. Jégo, R. Dasgupta, Fluid-present melting of sulfide-bearing ocean-crust: Experimental
665 constraints on the transport of sulfur from subducting slab to mantle wedge. *Geochim.*
666 *Cosmochim. Acta* **110**, 106-134 (2013).
- 667 69. T. Holland, R. Powell, An improved and extended internally consistent thermodynamic
668 dataset for phases of petrological interest, involving a new equation of state for solids. *J.*
669 *Metamorph. Geol.* **29**, 333-383 (2011).
- 670 70. G. S. Pokrovski *et al.*, Sulfur radical species form gold deposits on Earth. *Proc. Nat. Acad.*
671 *Sci.* **112**, 13484-13489 (2015).
- 672 71. K. Rauchenstein-Martinek, T. Wagner, M. Wälle, C. A. Heinrich, Gold concentrations in
673 metamorphic fluids: A LA-ICPMS study of fluid inclusions from the Alpine orogenic belt.
674 *Chem. Geol.* **385**, 70-83 (2014).
- 675 72. Y. V. Shvarov, HCh: New potentialities for the thermodynamic simulation of geochemical
676 systems offered by windows. *Geochem. Int.* **46**, 834-839 (2008).
- 677 73. J. C. M. de Hoog, P. R. D. Mason, M. J. van Bergen, Sulfur and chalcophile elements in
678 subduction zones: constraints from a laser ablation ICP-MS study of melt inclusions from
679 Galunggung Volcano, Indonesia. *Geochim. Cosmochim. Acta* **65**, 3147-3164 (2001).
- 680 74. Z. Zajacz, P. A. Candela, P. M. Piccoli, M. Wälle, C. Sanchez-Valle, Gold and copper in
681 volatile saturated mafic to intermediate magmas: Solubilities, partitioning, and implications
682 for ore deposit formation. *Geochim. Cosmochim. Acta* **91**, 140-159 (2012).
- 683 75. D. H. Green, W. O. Hibberson, I. Kovács, A. Rosenthal, Water and its influence on the
684 lithosphere–asthenosphere boundary. *Nature* **467**, 448-451 (2010).
- 685 76. K. Hattori, Porphyry copper potential in Japan based on magmatic oxidation state. *Resour.*
686 *Geol.* **68**, 126-137 (2018).
- 687 77. D. A. Holwell *et al.*, Mobilisation of deep crustal sulfide melts as a first order control on
688 upper lithospheric metallogeny. *Nat. Commun.* **13**, 573 (2022).
- 689 78. J. J. Wilkinson, Triggers for the formation of porphyry ore deposits in magmatic arcs. *Nat.*
690 *Geosci.* **6**, 917-925 (2013).

691

692 **Figures and Tables**

693

694 **Figure 1. Mineral assemblages and dominant sulfur species in the devolatilization fluid for**
695 **an average AOC along the hot (central Cascadia) and cold (central Honshu) subduction**
696 **pressure-temperature (P-T) paths. (A and B) Proportions (vol.%) of main minerals along the hot**
697 **(A) and cold (B) subduction geotherms. (C and D) Molality (mol/kg H₂O) of dominant sulfur aqueous**
698 **species along the hot (C) and cold (D) P-T paths. Temperature and corresponding slab depth are**
699 **both plotted along the x-axis. The vertical black dash lines mark the complete breakdown of the**
700 **dominant hydrous phases. Blue curves in (A) and (B) show the percentage of H₂O in solid hydrous**
701 **phases. Red stars show the boundary depth between lithosphere and asthenosphere beneath the**
702 **volcanic arc of a hot and cold subduction zone. Slab subduction P-T paths are from ref. (62). The**
703 **black, green and red open circles in (A) and (B) mark the extraction depths of fluids selected to**
704 **compute the mantle infiltration model (see Materials and Methods). The S₃⁻ ion is not shown in**
705 **panels C and D because of its concentrations < 10⁻⁴ mol/kg H₂O, due to too oxidizing conditions of**
706 **the slab devolatilization fluid. Mineral abbreviations: Ab–albite, Anh–anhydrite, Carb–carbonate,**
707 **Chl–chlorite, Coe–coesite, Cpx–clinopyroxene, Ep–epidote, Grt–garnet, Ky–kyanite, Lws–**
708 **lawsonite, Mus–muscovite, Fsp–feldspar, Pmp–pumpellyite, Py–pyrite, Qz–quartz, Stb–stilbite, Stp–**
709 **stilpnomelane, Tlc–talc.**

710

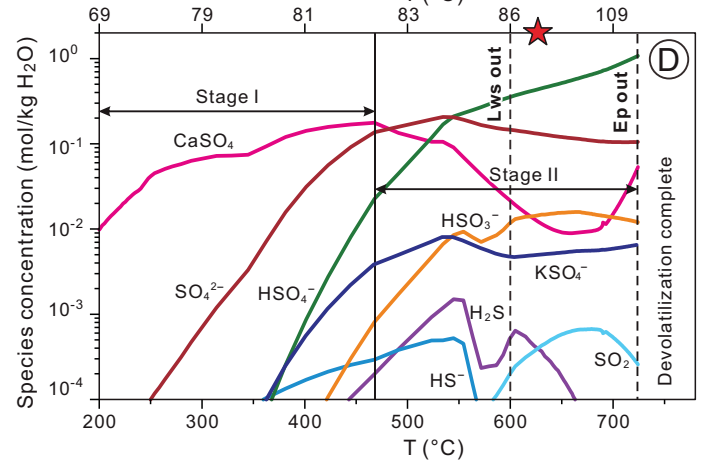
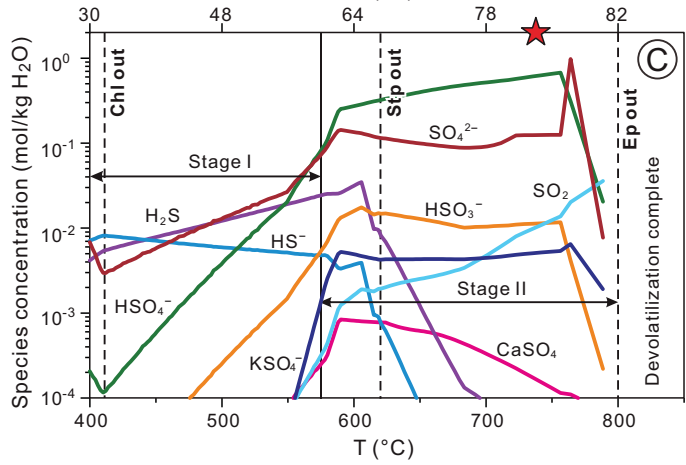
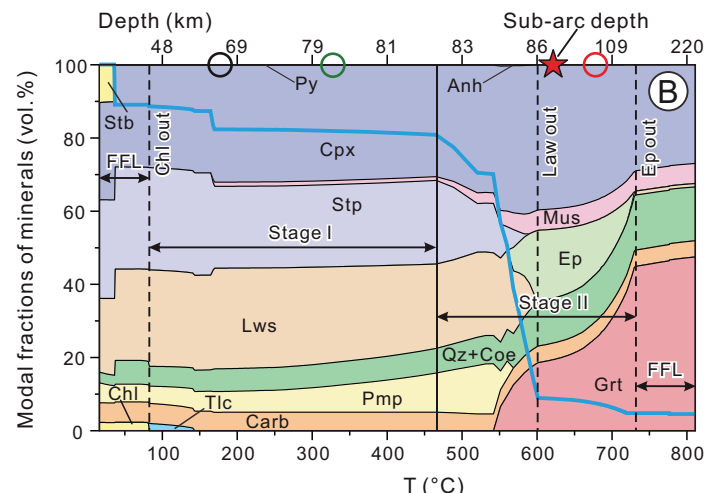
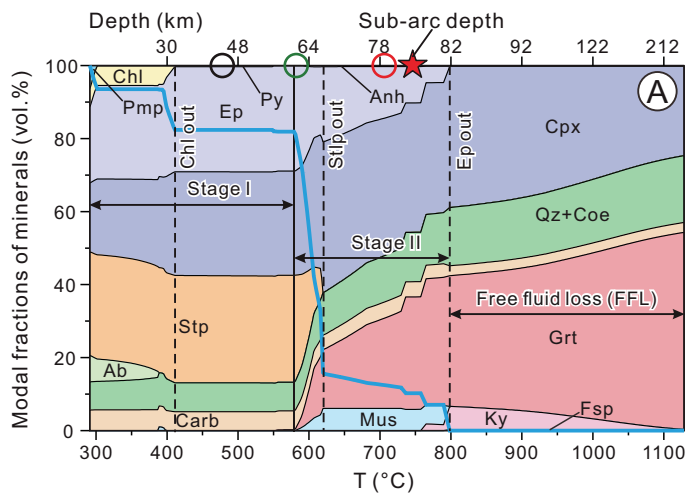
711 **Figure 2. Mantle wedge oxidation models showing the oxidation capacity of slab**
712 **devolatilization fluids. (A and B) The capacity of aqueous fluid containing different S⁶⁺**
713 **concentrations to oxidize the mantle wedge at near wet-solidus conditions is computed for a hot**
714 **(1000 °C, 2.4 GPa) and a cold (1000 °C, 3.3 GPa) subduction geotherm. (C and D) Variation of**
715 **oxygen fugacity (color coded) and stable mineral assemblages for T = 700–1100 °C and P = 2.4**
716 **and 3.3 GPa, computed by mixing depleted mantle peridotite and fluid released at sub-arc depth at**
717 **different fluid/rock mass ratios (non-linear scale, see Materials and Methods). Horizontal blue-**
718 **shaded region in (A) and (B) indicates the minimum range of oxygen fugacity of primitive arc melts**
719 **(16, 75). The oxygen fugacity of typical porphyry deposits (76) is indicated by gray-shaded field in**
720 **(A) and (B). Vertical lines with double-head arrows encompass the range of fO₂ values recorded in**
721 **arc magmas (76). Mineral abbreviations: Amp–amphibole, Anh–anhydrite, Bt–biotite, Chl–Chlorite,**
722 **Cpx–clinopyroxene, Dol–dolomite, F–fluid, Grt–garnet, Mgs–magnesite, Ol–olivine, Opx–**
723 **orthopyroxene, Pyh–pyrrhotite, Py–pyrite.**

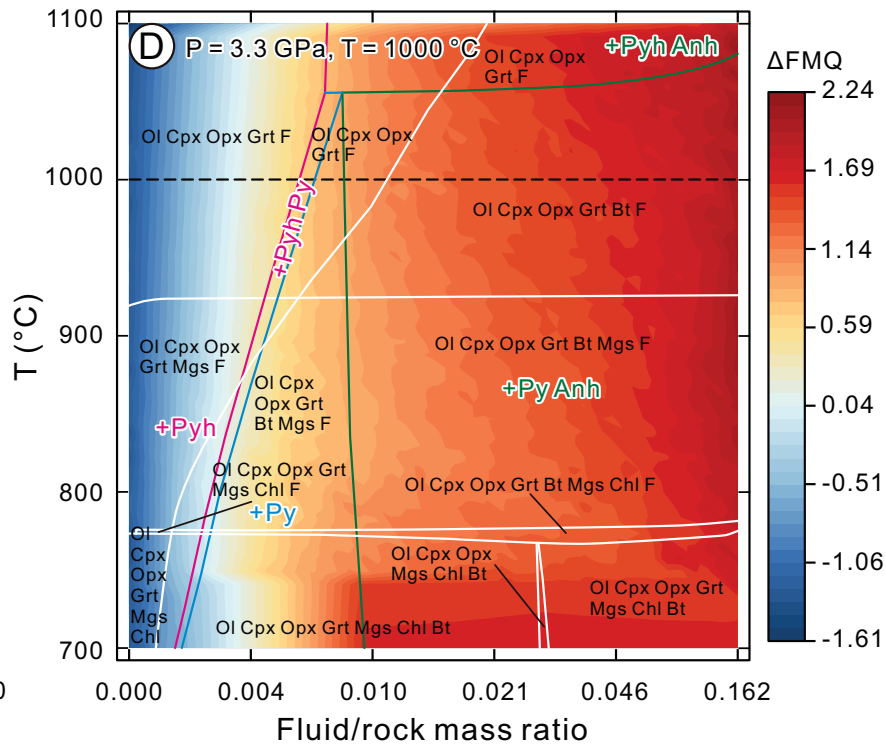
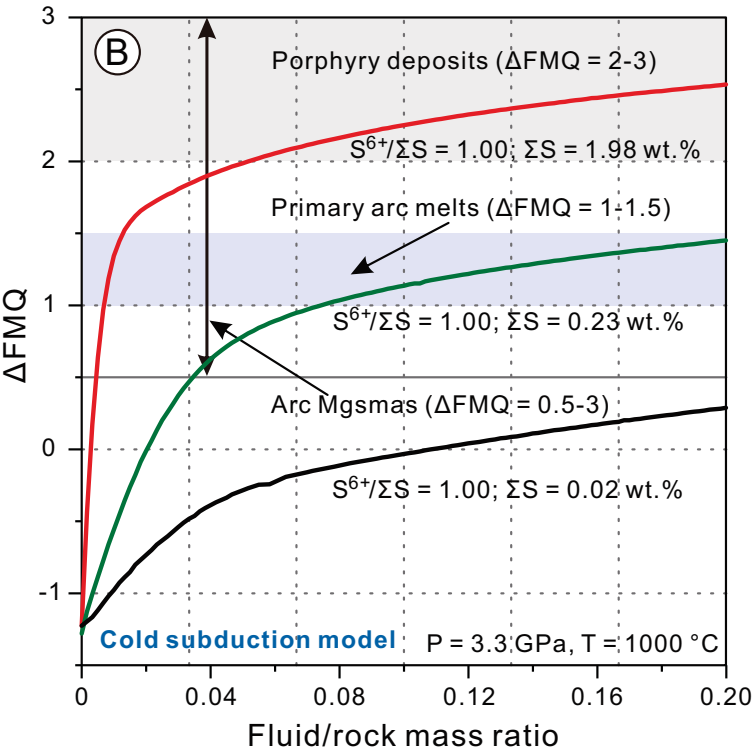
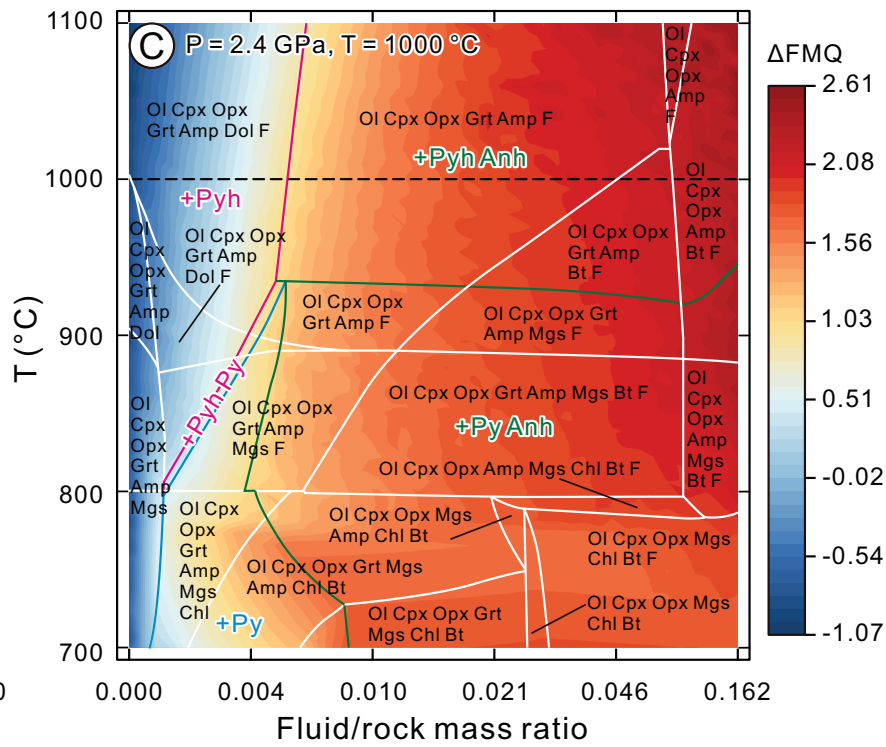
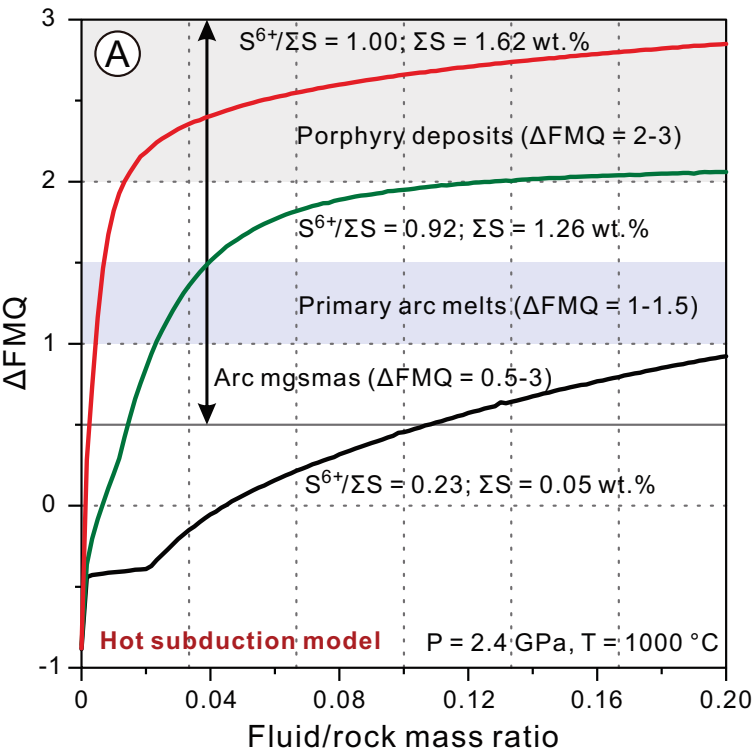
724

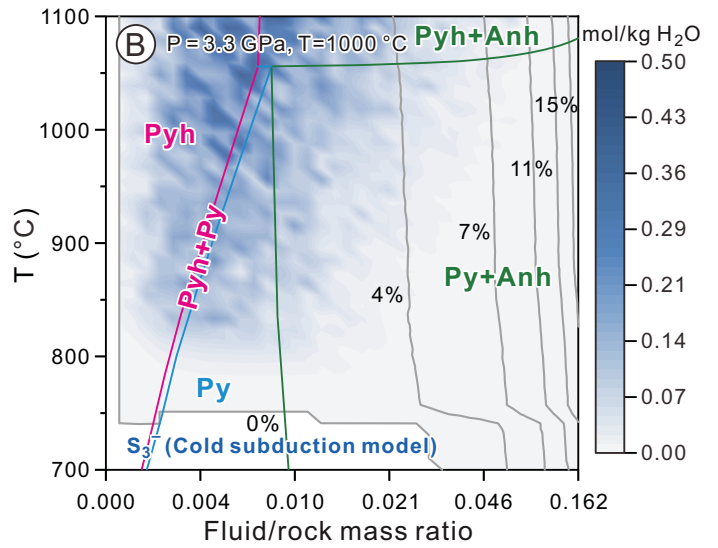
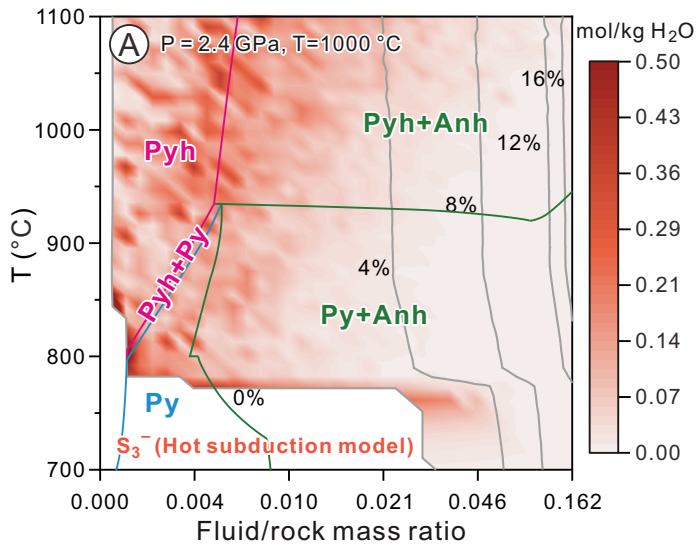
725 **Figure 3. Distribution of S₃⁻ ion and indicated gold aqueous species in slab-derived fluid**
726 **upon reaction with mantle peridotite. (A and B) Orange and blue contour maps show molality of**
727 **S₃⁻ computed for the hot and cold subduction model, respectively. Color curves outline the phase**
728 **boundaries of S-bearing minerals as a function of fluid/rock ratio (non-linear scale, see Materials**
729 **and Methods). Gray contours state for the weight percent (wt.%) of fluid in the fluid-rock system.**
730 **The color bar on the right of each panel shows the concentrations of S₃⁻. (C) Variations of gold**
731 **aqueous species concentrations as a function of oxygen fugacity at pH ~5 as buffered by the**
732 **olivine-pyroxene-garnet mantle rock assemblage at a fluid/rock mass ratio of 0.1. The vertical**
733 **dashed lines show the log₁₀(fO₂) values of the fayalite-magnetite-quartz (FMQ), pyrite-pyrrhotite-**
734 **magnetite (PPM) and hematite-magnetite (HM) conventional redox buffers. The oxygen fugacity of**
735 **metasomatized mantle (from FMQ to ΔFMQ+2) is marked by vertical blue-shaded region (11). (D)**
736 **The effects of total dissolved sulfur concentration on the equilibrium distribution of gold aqueous**
737 **species calculated for subducted slab-derived metamorphic fluid at pH of 5 and fO₂ of the H₂S-SO₂**
738 **equilibrium (corresponding to ΔFMQ+1.5). The horizontal lines with double-head arrows and vertical**
739 **blue-shaded region display the sulfur contents of aqueous fluid as constrained by experiments from**
740 **ref. (68).**

742 **Figure 4. Estimated total Au contents in fluid and silicate melt during hydrous mantle**
743 **melting at different redox conditions. (A and B)** Fractions of total Au in the fluid and melt as a
744 function of degree of melting (F) and at different aqueous fluid contents at low-temperature melting
745 in the stability field of MSS at redox conditions of $\Delta\text{FMQ}-1.0$ and $\Delta\text{FMQ}+1.5$. **(C and D)** Total gold
746 fractions released into both the fluid and silicate melt (C) as a function of F value and for high-
747 temperature partial melting in the presence of sulfide liquid at $\Delta\text{FMQ}-1.0$ (C) and $\Delta\text{FMQ}+1.5$ (D).
748 The vertical, blue-shaded region defines a low-degree melting range, typically of 5% for
749 lamprophyre. Fluid proportions indicated in all panels represent the assumed fraction of the free
750 aqueous fluid of the system. The Au content released into the fluid and melt is simulated by mass
751 balance and using experimentally available Au partition coefficients (see Materials and Methods).
752

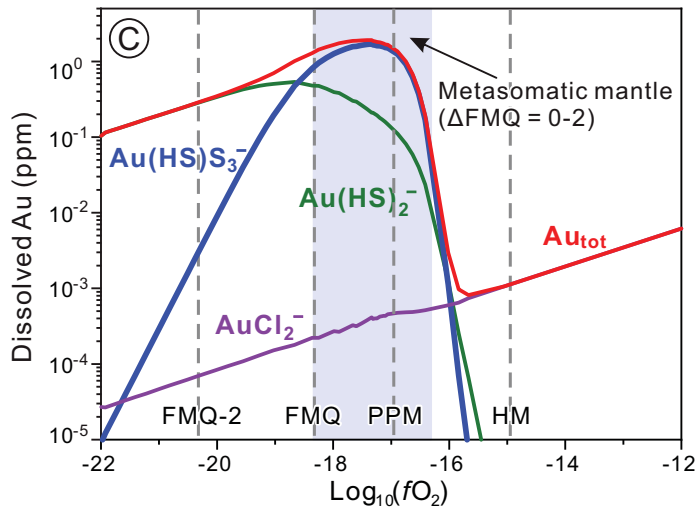
753 **Figure 5. Proposed scenarios for progressive devolatilization and redox processes at slab-**
754 **mantle interface. (A)** Schematic profile of a subduction zone with associated metamorphic
755 devolatilization and magmatism (modified from (77) and (78)) showing the redox conditions and
756 mobilization and concentration of sulfur and gold during mantle metasomatism as derived in this
757 study. The white stars mark the slab depths of fore-arc and sub-arc settings. **(B)** Schematic
758 representation of a slab-derived fluid oxidizing overlying mantle wedge and concentrating sulfur and
759 gold. The fluid liberated from AOC carries abundant S^{6+} into the mantle wedge to oxidize Fe^{2+} in
760 silicate minerals, thereby modifying the mantle oxidation state and leading to gold enrichment in the
761 fluid due to reduction of S^{6+} to S_3^- and $\text{H}_2\text{S}/\text{HS}^-$ ligands that strongly complex gold. Mineral
762 abbreviations: Px–pyroxene; Grt–garnet; Ol–olivine.







600 °C, 1.5 GPa, 3 wt% S,
5 wt% NaCl, pH = 5.0, $\Delta\text{pH} = 1.5$



600 °C, 1.5 GPa, $\text{H}_2\text{S}/\text{SO}_2 = 1:1$,
5 wt% NaCl, pH = 5.0, $\Delta\text{pH} = 1.5$

